Journal of
Biomedical Optics

SPIEDigitalLibrary.org/jbo

Estimating the absorption coefficient of the bottom layer in four-layered turbid mediums based on the time-domain depth sensitivity of near-infrared light reflectance

Chie Sato
Miho Shimada
Yukari Tanikawa
Yoko Hoshi

Journal of Biomedical Optics 18(9), 097005 (September 2013)

Estimating the absorption coefficient of the bottom layer in four-layered turbid mediums based on the time-domain depth sensitivity of near-infrared light reflectance

Chie Sato,[a] Miho Shimada,[b] Yukari Tanikawa,[c] and Yoko Hoshi[a]
[a]Tokyo Metropolitan Institute of Medical Science, Integrated Neuroscience Research Project, 2-1-6 Kamikitazawa, Setagaya-ku, Tokyo 156-8506, Japan
[b]High Energy Accelerator Research Organization, Accelerator Laboratory, 1-1 Oho, Tsukuba 305-0801, Japan
[c]National Institute of Advanced Industrial Science and Technology, Biomedical Sensing and Imaging Group, 1-2-1 Namiki, Tsukuba 305-8564, Japan

Abstract. Expanding our previously proposed "time segment analysis" for a two-layered turbid medium, this study attempted to selectively determine the absorption coefficient (μ_a) of the bottom layer in a four-layered human head model with time-domain near-infrared measurements. The difference curve in the temporal profiles of the light attenuation between an object and a reference medium, which are obtained from Monte Carlo simulations, is divided into segments along the time axis, and a slope for each segment is calculated to obtain the depth-dependent μ_a (μ_a^{seg}). The reduced scattering coefficient ($\mu_s{}'$) of the reference is determined by curve fitting with the temporal point spread function derived from the analytical solution of the diffusion equation to the time-resolved reflectance of the object. The deviation of μ_a^{seg} from the actual μ_a is expressed by a function of the ratio of μ_a^{seg} in an earlier time segment to that in a later segment for mediums with different optical properties and thicknesses of the upper layers. Using this function, it is possible to determine the μ_a of the bottom layer in a four-layered epoxy resin-based phantom. These results suggest that the method reported here has potential for determining the μ_a of the cerebral tissue in humans. [DOI: 10.1117/1.JBO.18.9.097005]

Keywords: near-infrared spectroscopy; time-resolved spectroscopy; depth-dependent μ_a; layered turbid medium.

Paper 130306RR received May 2, 2013; revised manuscript received Aug. 26, 2013; accepted for publication Aug. 28, 2013; published online Sep. 20, 2013.

1 Introduction

In 1977, Jöbsis[1] was the first to report near-infrared measurements of tissue oxygenation in living animals, and near-infrared spectroscopy (NIRS) has been developing into a useful tool for monitoring of cerebral hemodynamic changes. Today, NIRS is used in a wide variety of research fields and in clinical medicine, while quantitative and selective extraction of signals originating in the brain remains difficult. Recently, there have been reports that the skin blood flow influences NIRS signals, an issue that cannot be ignored in NIRS studies.[2,3] Over the past 35 years, the NIRS community has focused on solving these issues and has developed a wide range of types of NIRS measurements. Among these, time-domain measurement [time-resolved spectroscopy (TRS)] is a very promising approach to these issues, as TRS provides a temporal profile of the detected light intensity [temporal point spread function (TPSF)], which carries information about depth-dependent attenuation based on the correlation of detection time and penetration depth of photons (time-domain depth sensitivity).[4–7]

Propagation of photons in living tissue is described by the radiative transport equation (RTE); however, the RTE, an integro-differential equation, is not easy to solve even by numerical methods. Therefore, a diffusion approximation to the RTE is widely used instead, since light propagation can be considered isotropic at the macroscopic level, when the scattering interaction is much larger than the absorption and the point of interest is far from light sources and boundaries.[8] In conventional time-domain measurements of the human head, the absorption coefficient (μ_a) of the cerebral tissue has commonly been determined by fitting the TPSF derived from an analytical solution of the photon diffusion equation (DE) to the profile of the time-resolved reflectance on the assumption that the head is semi-infinite and homogeneous.[9–11] This approach selectively measures cerebral optical properties, but the selective and quantitative accuracies are inadequate because of limitations of the diffusion approximation to the RTE for inhomogeneous biological tissue.[12–14] Other methods have also been proposed to estimate the optical properties of layered mediums, such as the multilayered (time-dependent) DE,[15–17] also a method with spatially and time-resolved reflectance,[18] and a method considering time-dependent mean partial path lengths.[19] However, none of these methods have been applied to practical human head measurements.

Diffuse optical tomography (DOT) is a technique for reconstructing images of optical properties using multiple light sources and detectors[20] and is thought to be the most promising technique for the quantitative detection of focal changes in cerebral hemodynamics. DOT can be performed with time-domain,[21] frequency-domain,[22] and continuous-wave (CW) measurement instruments.[23] Recently, CW high-density DOT with high spatial resolution has been developed and applied to functional hemodynamic maps of the adult human visual cortex.[24] However, this CW-DOT only provides qualitative images

---

Address all correspondence to: Yoko Hoshi, Tokyo Metropolitan Institute of Medical Science, Integrated Neuroscience Research Project, 2-1-6 Kamikitazawa, Setagaya-ku, Tokyo 156-8506, Japan. Tel: 81-3-5316-3100x1240; Fax: 81-3-5316-3150; E-mail: hoshi-yk@igakuken.or.jp

of the measured changes as it is based on linear image reconstruction. Nonlinear iterative reconstruction schemes are required to obtain quantitative images, and such procedures are still under development.[25]

We have previously proposed a novel approach, "time segment analysis," for determination of the μ_a of each layer in a two-layered turbid medium with a single-channel TRS instrument.[26] In that approach, first a time-attenuation difference curve, derived by the subtraction of the time-resolved reflectance of a reference medium from that of an object, was divided into segments along the time axis (e.g., 500 ps time width). Then, a depth-dependent μ_a (time-segmented μ_a) was estimated from the slope of each segment. The difference between the estimated μ_a and the actual μ_a in the lower layer then depends on the ratio of the actual μ_a in the upper layer to that in the lower layer, which was linearly related to the ratio of the estimated μ_a in an early time segment to that in a later segment. Using this relationship, it was possible to correct the μ_a obtained from the later time segment to derive the μ_a of the lower layer in two-layered mediums. An advantage of this approach is that it involves a single-distance measurement, which is more suitable than a multidistance measurement for measurements of the head with its heterogeneous superficial layer and curvature. A single distance measurement is also straightforward to expand into multichannel measurements. To apply our method to human head measurements, the validity and reliability of the method must be confirmed with three or more layered models and with other models with more complex structures. In the present study, the investigation focuses on the applicability of our method[26] to a four-layered slab model with a Monte Carlo simulation and phantom experiments.

The article here first reports the results of simulations: (1) time-segmented μ_a under several conditions in which μ_a and the reduced scattering coefficient ($\mu_s{}'$) of each layer were changed, (2) the difference between the time-segmented μ_a at a later time and the actual μ_a of the bottom layer, and its relation to the ratio of the time-segmented μ_a in an earlier time segment to that of a later one, and (3) the mean partial path length of photons detected in each time segment to be able to interpret the time-segmented μ_a values. Then, the experimental results are reported: (4) the determination of μ_a of the bottom layer of a four-layered epoxy resin-based phantom with the "time segment analysis."

2 Methods for Determining the μ_a of the Bottom Layer

The details of the method have been described in a previous paper,[26] and the following is a brief summary.

2.1 *Theoretical Basis*

Two kinds of mediums, a reference medium and an object medium for the measurements, are considered. When a light impulse is irradiated on the surface of the mediums, the reflected light intensity at time t for the reference and the object is expressed by $I_R(t) = S_R(t)\exp(-\mu_{a,R}\cdot c_R\cdot t)$ and $I(t) = S(t)\exp(-\mu_a\cdot c\cdot t)$,[27,28] where c is the light velocity in a medium and $S(t)$ is a scattering function which is dependent on the $\mu_s{}'$ of the medium in the photon diffusion regime. The light attenuation, A, is defined as the logarithm of the inverse of the reflectance. According to the time-resolved Beer–Lambert law, the difference between the attenuation of an object $[A(t)]$ and of a reference $[A_R(t)]$, $A^{\mathrm{diff}}(t)$, can be expressed by

$$\begin{aligned}A^{\mathrm{diff}}(t) &= A(t) - A_R(t) = \ln[I_R(t)/I(t)]\\ &= (\mu_a\cdot c - \mu_{a,R}\cdot c_R)t + S^{\mathrm{diff}}(t),\end{aligned}\tag{1}$$

where $S^{\mathrm{diff}}(t) = \ln[S_R(t)/S(t)]$.

In the case of an object that is a layered medium in which μ_a varies with layer (i.e., depth) and the reference is homogeneous, $A^{\mathrm{diff}}(t)$ is not a linear function of t even though $S^{\mathrm{diff}}(t)$ can be ignored and $c = c_R$, that is, μ_a is different at each detection time. The method introduces a time-dependent apparent absorption coefficient, $\mu_a(t)$, given by $\sum_i \mu_{ai} l_i(t)/L(t)$, where the subscript i refers to the i'th layer in the object medium, $l_i(t)$ is the stochastic time-dependent partial path length in the i'th layer for the photons detected at time t, and $L(t)$ is the total path length of photons detected at time t, which is defined as $L(t) = ct$. Then $\mathrm{d}A^{\mathrm{diff}}(t)/\mathrm{d}t$ is expressed as follows:

$$\begin{aligned}\mathrm{d}A^{\mathrm{diff}}(t)/\mathrm{d}t &= (\mathrm{d}/\mathrm{d}t)[\mu_a(t)ct - \mu_{a,R}\cdot c_R\cdot t] + \mathrm{d}S^{\mathrm{diff}}(t)/\mathrm{d}t\\ &= \sum_i [\mu ai\cdot \mathrm{d}li(t)/\mathrm{d}t] - \mu_{a,R}\cdot c_R + \mathrm{d}S^{\mathrm{diff}}(t)/\mathrm{d}t,\end{aligned}\tag{2}$$

where $\mathrm{d}A^{\mathrm{diff}}(t)/\mathrm{d}t$ expresses the variation of μ_a in the depth direction in the object.

2.2 *Time Segment Analysis*

To simplify the process of the analysis, the $A^{\mathrm{diff}} - t$ curve within a short time range (e.g., a few hundred picoseconds, Δt) is considered a straight line, and a term for the mean absorption differences, $\langle \mathrm{d}A^{\mathrm{diff}}(t)/\mathrm{d}t\rangle$, is introduced, the value of this is obtained by $\Delta A^{\mathrm{diff}}(t)/\Delta t$, rather than $\mathrm{d}A^{\mathrm{diff}}(t)/\mathrm{d}t$. In this study, the $A^{\mathrm{diff}} - t$ curve in the range 500 to 3500 ps is divided into six time segments of 500 ps, and the slope of each time segment is estimated ($\langle \mathrm{d}A^{\mathrm{diff}}(t)/\mathrm{d}t\rangle$) by linear regression. The mean $\mu_a(t)$ of each time segment is referred to as the time-segmented μ_a, μ_a^{seg}. Then, assuming that a reference and an object have the same $\mu_s{}'$ and refractive index, this gives the following equation,

$$\langle \mathrm{d}A^{\mathrm{diff}}(t)/\mathrm{d}t\rangle = (\mu_a^{\mathrm{seg}} - \mu_{a,R})c.\tag{3}$$

The time-segmented $\mu_a(\mu_a^{\mathrm{seg}})$ was calculated by substituting $\langle \mathrm{d}A^{\mathrm{diff}}(t)/\mathrm{d}t\rangle$, μ_a, R, and c in Eq. (3).

The segments of the $A^{\mathrm{diff}} - t$ curve were numbered as $K = \mathrm{I}, \mathrm{II}, \ldots, \mathrm{VI}$ in time order, so the segment of a time range from 500 to 1000 ps is referred to as segment-I and that from 2500 to 3000 ps was as segment-V, μ_a^{seg} (K) denotes the μ_a^{seg} in segment K.

3 Simulation and Experiment

3.1 *Monte Carlo Simulations – Calculation of the Time-Resolved Reflectances*

To calculate the reflectances from four-layered (object) and from homogeneous (reference) mediums, we used the Monte Carlo code developed by Wang and Jacques.[29] The code was modified to fit our measurement system. Source photons were perpendicularly irradiated onto the surface of the semi-infinite mediums, and photons that were emitted from a detector position on the surface were all detected with a time step of 10 ps, and the source–detector distance was 30 mm. Reflectance profiles simulated in an anisotropic setting (scattering coefficient $\mu_s = 10\ \mathrm{mm}^{-1}$, anisotropy parameter $g = 0.9$), were compared with those in an isotropic setting ($\mu_s = 1.0\ \mathrm{mm}^{-1}$) and it was confirmed that the differences between the two were small enough to be disregarded in these simulating parameter conditions. Thus, an isotropic scattering was assumed, reducing the calculation time, and the calculations were repeated until the number of detected photons reached 1,000,000. A light velocity of 0.219 mm/ps (refractive index 1.37) was used in all the calculations.

In the previous study,[26] we confirmed that temporal profiles of detected light intensity in homogeneous and two-layered phantoms, which consisted of two layers with optical properties the same as those of the homogeneous one, were almost in agreement. Thus, the effect of the interface between two layers on the pattern of photon propagation was considered to be negligible in the Monte Carlo simulation and phantom measurement under present study conditions.

The statistical error of the Monte Carlo simulation was estimated by fitting a theoretical TPSF for a semi-infinite homogenous medium (based on the solution of the DE derived by employing the extrapolated boundary condition of the reflectance mode[30–32]) to the TPSF obtained from the Monte Carlo simulation (time range of 0 to 4500 ps). The photon diffusion coefficient was expressed by $D = 1/3\mu_s{}'$.[33] In the fitting procedure, a weighted least squares fitting method based on the Levenberg–Marquardt Method,[34,35] which is an iterative improved method, was used. In case of practical TRS measurements of inhomogeneous objects, such as the human head, when the chi square nu (χ_ν^2) value is 0.7 to 1.3, it is considered that the theoretical TPSF is well fitted to the observed one.[36,37] In the present study, it was assumed that the best fitting TPSF was the reference true solution, and that the χ_ν^2 value mainly represented statistical bias and statistical variations that were attributed to the Monte Carlo simulation. The χ_ν^2 values in all the mathematical models described in Sec. 3.2 (Table 1) were 1.09 ± 0.05 (mean ± SD). Thus, it was concluded that the statistical error of the Monte Carlo simulation was negligible.

3.2 *Four-Layered Models for Simulation*

We used a four-layered semi-infinite model as a human head model. The layers are numbered $i = 1, 2, 3$, and 4 in order of depth from the outside, and denoted by #i: the layers #1 to #4 correspond to the scalp, skull, cerebrospinal fluid (CSF), and brain, respectively. The $\mu_s{}'$, μ_a, and the thickness d of each layer are denoted by $\mu_{si}{}'$, μ_{ai}, and d_i, respectively. Table 1 shows the values used in this paper. The optical properties of each layer were chosen from the published data.[7,38,39] The depth from the scalp to the cortical surface was set to 9.0 to 15.0 mm in the forehead region.[40–42]

The models were classified into three groups according to the $\mu_{s1}{}'$ and $\mu_{s2}{}'$ values: 1.3 and 1.0 mm^{-1} for Group A, 1.1 and 0.8 mm^{-1} for Group B, and 1.8 and 1.2 mm^{-1} for Group C. The $\mu_{s3}{}'$ and $\mu_{s4}{}'$ values were set to 0.1 and 1.7 mm^{-1} in all three groups. In Group A, μ_a was varied in the range of 0.013 to 0.02 mm^{-1} in layer #1, 0.011 to 0.014 mm^{-1} in layer #2, and 0.01 to 0.02 mm^{-1} in layer #4 separately. In Groups B and C, only μ_{a1} and μ_{a4} were varied and μ_{a2} was set to 0.012 mm^{-1}. In all the models, μ_{a1} was set to be larger than μ_{a2} as the μ_a of the scalp is generally larger than that of the skull in adult heads,[43–45] and μ_{a3} was 0.0033 mm^{-1}. The thicknesses of layers #1 and #2, (d_1, d_2) (mm), were set to (3, 5), (3, 7), (4, 7), (5, 7), (5, 5), or (5, 9) in Group A, (3, 7) or (5, 7) in Group B, and (5, 7) in Group C, whereas d_3 and d_4 were set as 1 and 90 mm, respectively. We mainly evaluated temporal variations in μ_a^{seg} and differences between μ_a^{seg} and the actual μ_a for the Group A models. The models in Groups B and C were used to investigate the effects of the $\mu_s{}'$ variation in the upper layers on μ_a^{seg}. The $\mu_s{}'$ of the homogeneous reference was changed within the range of 1.1 to 1.8 mm^{-1} as described below, while the μ_a and the thickness were set to 0 mm^{-1} and 100 mm, respectively.

Table 1 Optical properties and layer thickness of four layered models used in simulation.

Layer (#)	$\mu_s{}'$ (mm^{-1})	μ_a (mm^{-1})	d (mm)
Group A			
1	1.3	0.0013–0.02	$(d_1, d_2) = (3, 5)$, (3, 7),
2	1.0	0.011–0.014	(4, 7), (5, 7), (5, 5), (5, 9)
3	0.1	0.0033	1
4	1.7	0.01–0.02	90
Group B			
1	1.1	0.0013–0.02	$(d_1, d_2) = (3, 7)$, (5, 7)
2	0.8	0.012	
3	0.1	0.0033	1
4	1.7	0.01–0.02	90
Group C			
1	1.8	0.0013–0.02	$(d_1, d_2) = (5, 7)$
2	1.2	0.012	
3	0.1	0.0033	1
4	1.7	0.01–0.02	90

3.3 *Determination of $\mu_s{}'$ for the Reference Mediums*

In the previous study,[26] it was found that the results of our method depend on the $\mu_s{}'$ value of the reference, which was ideally the same as that of the upper layer of a two-layered object medium. In general, the $\mu_s{}'$ value of a multilayered medium determined by the curve fitting procedure as described in Sec. 3.1 is closer to the $\mu_s{}'$ of the upper layer than that of the lower layer. This can be explained by the fact that the slope of the rising phase of the TPSF is dependent on the $\mu_s{}'$ value but independent of the μ_a value, when the optical properties are in the range of the published data for the biological tissue.[46] In this article, the $\mu_s{}'$ value of the reference was determined by curve fitting with the TPSF derived from an analytical solution of the DE for a semi-infinite homogenous medium to the profile of the time-resolved reflectance of the object medium in the time range of 250 to 1000 ps. The reason why we chose this time range is described in Discussion (Sec. 5.2).

3.4 *Calculation of Mean Partial Path Lengths*

As shown in Eqs. (2) and (3), μ_a^{seg} depends on the temporal change in $l_i(t)$ in the time range of each segment in each layer. Therefore, to interpret the calculated μ_a^{seg}, the mean partial path lengths in each layer for a four-layered medium were also estimated by the Monte Carlo simulation. Two models in Group A [$\mu_{a1} = 0.015, \mu_{a2} = 0.012, \mu_{a4} = 0.02, (d_1, d_2) = (5, 5)$; and $\mu_{a1} = 0.015$, $\mu_{a2} = 0.012$, $\mu_{a4} = 0.01$, $(d_1, d_2) = (5, 5)$], were perpendicularly partitioned into 1 mm thick laminae and the attenuation changes (ΔA) caused by altering μ_a in a lamina by $+10\%$ of the initial value were calculated. The time-independent mean partial path length of photons in the lamina where μ_a is changed can be estimated by the $\Delta A/\Delta\mu_a$ of the whole time range of the time-resolved reflectance. The present study estimated a time-dependent mean partial path length given by the time segment unit [denoted as the time-segment dependent mean partial path length (s-mPPL)] at the depth of z to $z + 1$ mm ($z = 0, 1, 2, \dots, 19$) obtained by dividing the ΔA calculated in each time segment by $\Delta\mu_a$. We also calculated a time-segment dependent mean total path length (s-mTPL) in the medium, the product of the light velocity and the mean time of flight of photons in each time segment.

3.5 *Epoxy Resin-Based Phantoms*

Four-layered (object) and homogeneous (reference) phantoms, $140 \times 140 \times 63$ (50 for the reference) mm, were prepared. The base of the phantoms was epoxy resin (Beuhler, Lake Bluff, Illinois). We adjusted the $F_s{}'$ and μ_a to 0.1 to 1.77 and 0.0033 to 0.015 mm^{-1} at 760 nm, respectively, by adding titanium oxide (Tian Kogyo, Ube, Japan) as scatterers and ink (Greenish brown: Chugai Pharmaceutical, Tokyo, Japan) as an absorber. The thickness of each layer and the optical properties of the object are shown in Table 2. These optical properties are theoretical values based on the concentrations of titanium oxide and ink. Unlike the mathematical phantoms, there were no differences in the $\mu_s{}'$ values of the objects determined in the two time ranges used in the fitting (1.520 mm^{-1}, 250 to 1000 ps; and 1.502 mm^{-1}, 0 to 4500 ps). The μ_a and $\mu_s{}'$ of the reference were 0.001 and 1.52 mm^{-1}, respectively (Table 2).

Table 2 Optical properties at 760 nm and layer thickness of epoxy resin-based phantoms, where $\mu_s{}'$ and F_a are theoretical values based on the concentration of titanium oxide and ink.

Layer (#)	$\mu_s{}'$ (mm^{-1})	μ_a (mm^{-1})	d (mm)
		Object	
1	1.36	0.016	4
2	1.0	0.012	6
3	0.1	0.0033	3
4	1.77	0.015	50
		Reference	
1	1.52	0.001	50

3.6 *Instrumentation*

A two-channel TRS instrument (TRS-20, Hamamatsu Photonics, Hamamatsu, Japan) was employed. The TRS-20 consists of three pulsed laser diodes with different wavelengths (760, 800, and 830 nm) with durations of around 150 ps [full width at half maximum (FWHM)] at the repetition rate of 5 MHz, a high-speed photomultiplier tube for single photon detection, and a circuit for time-resolved measurements based on a time correlated single photon counting method. Incident light is delivered to the sample through an optical light guide [GI type, 200 μm core diameter, numerical aperture (NA) $=$ 0.25]. Reflected light is collected by a fiber bundle (3-mm diameter, NA $= 0.26$). Minimum data acquisition time is 100 ms.

3.7 *Time-Resolved Measurements of a Phantom*

The incident and detecting light guides were placed on the upper surface of a phantom, separated by 30 mm. Measurements with an accumulated time of 10 s were conducted at five different positions within an area 40 mm from the edge of the phantom to avoid the distortion of photon propagation due to the edge. Specular reflection and light leakage were prevented with a black light-guide holder. Instrument responses of TRS-20 were measured by placing the incident fiber opposite the detecting fiber with a neutral density filter between the two. The instrument response of was around 250 ps FWHM at all wavelengths.

The optical properties of the phantoms were determined by curve fitting with the TPSF derived from an analytical solution of the DE with the extrapolated boundary condition, convoluted by the instrument function to the measured profile of the time-resolved reflectance as described in Sec. 3.1. The light velocity in the phantoms was assumed to be 0.19 mm/ps, corresponding to a refractive index of 1.58. Before the calculation of $A^{\text{diff}}(t)$, the profiles of the time-resolved reflectance measured by TRS were deconvoluted by the instrument function by using Bayesian deconvolution.[47]

4 Results

4.1 *Temporal Variations in μ_a^{seg}*

Figure 1 shows the temporal variations in μ_a^{seg} obtained from the nine models in Group A. Figure 1(a) shows results in the mediums where both μ_{a1} and μ_{a2} were larger than μ_{a4} (squares) and where μ_{a1} was larger but μ_{a2} was equal to μ_{a4} (triangles). Figure 1(b) shows results in the mediums where μ_{a2} was smaller than FFFF_{a4} and μ_{a1}, while μ_{a1} were larger than (diamonds), equal to (crosses), or smaller than μ_{a4} (circles). The μ_a^{seg} values are expressed as the ratio to μ_{a4}. When both μ_{a1} and μ_{a2} were larger than μ_{a4} [squares in Fig. 1(a)], the ratios of the μ_a^{seg} to the μ_{a4} [$\mu_a^{\text{seg}}(k)/\mu_{a4}$] term were above 1 in all the time segments. The values gradually decreased to become close to 1 as the time segments become later, and reached a value slightly larger than μ_{a4}. When μ_{a2} was equal to μ_{a4} [triangles in Fig. 1(a)], $\mu_a^{\text{seg}}(k)/\mu_{a4}$ is nearest 1 in the time segments later than IV. For all the models in Fig. 1(a), the upper layer thickness (d_1, d_2) influenced the values of μ_a^{seg} in segments-I and -II but not those in the later segments.

In the models where μ_{a2} was smaller than μ_{a4} [Fig. 1(b)], the $\mu_a^{\text{seg}}(k)/\mu_{a4}$ in all the time segments later than segment-II were smaller than 1. When μ_{a1} was equal to or larger than μ_{a4}, the μ_a^{seg} was almost constant in segments-II to -VI, and a little smaller

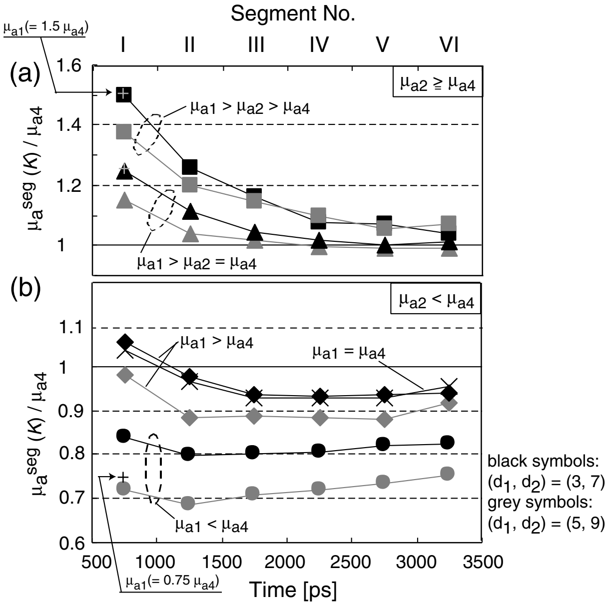

Fig. 1 Temporal variations of μ_a^{seg} of four-layered mediums (Group A) with two different sets of (d_1, d_2) predicted by Monte Carlo simulation. $(d_1, d_2) = (3, 7)$ (black symbols) and $(d_1, d_2) = (5, 9)$ (gray symbols). (a) μ_a^{seg} in the models where both μ_{a1} and μ_{a2} are larger than μ_{a4} (black filled square, gray filled square; $\mu_{a1} = 0.015\ \mathrm{mm}^{-1}$, $\mu_{a2} = 0.012\ \mathrm{mm}^{-1}$, $\mu_{a4} = 0.01\ \mathrm{mm}^{-1}$), and μ_{a1} is larger than and μ_{a2} is equal to μ_{a4} (black filled triangle, gray filled triangle; $\mu_{a1} = 0.015\ \mathrm{mm}^{-1}$, $\mu_{a2} = 0.012\ \mathrm{mm}^{-1}$, $\mu_{a4} = 0.012\ \mathrm{mm}^{-1}$). (b) μ_a^{seg} in the models where μ_{a2} is smaller than μ_{a4}, while μ_{a1} is larger than (black filled diamond, gray filled diamond; $\mu_{a1} = 0.018\ \mathrm{mm}^{-1}$, $\mu_{a2} = 0.012\ \mathrm{mm}^{-1}$, $\mu_{a4} = 0.015\ \mathrm{mm}^{-1}$), equal to ($\mu_{a1} = 0.015\ \mathrm{mm}^{-1}$, $\mu_{a2} = 0.012\ \mathrm{mm}^{-1}$, $\mu_{a4} = 0.015\ \mathrm{mm}^{-1}$), and smaller than (black filled circle, gray filled circle; $\mu_{a1} = 0.015\ \mathrm{mm}^{-1}$, $\mu_{a2} = 0.012\ \mathrm{mm}^{-1}$, $\mu_{a4} = 0.02\ \mathrm{mm}^{-1}$) μ_{a4}. The vertical axis represents the ratio of μ_a^{seg} to μ^{a4} ($\mu_a^{\mathrm{seg}}(\mathrm{k})/\mu_{a4}$).

than the μ_{a4} values. The values of μ_a^{seg} in the later time segments were independent of the value of μ_{a1}. When both μ_{a1} and μ_{a2} were smaller than μ_{a4}, the $\mu_a^{\mathrm{seg}}(k)/\mu_{a4}$ values were much smaller than one in all the time segments. The μ_a^{seg} decreased between segments I and II, then μ_a^{seg} increased slightly in the later time segments, and remained about 20% smaller than μ_{a4}. For all the models in Fig. 1(b), the differences between μ_{a4} and μ_a^{seg} in the later time segments were larger in the medium with $(d_1, d_2) = (5, 9)$ than in that with (3, 7). Further, the μ_a^{seg} values of the medium with (5, 9) were smaller than those of the medium with (3, 7) in all segments. The same tendency of the temporal variations of μ_a^{seg} was observed in other models with different sets of μ_{ai} and thicknesses.

4.2 *Differences Between the μ_a^{seg} and the Actual μ_a in the Bottom Layer*

In the previous study of two-layered models, it was found that the ratio of μ_a^{seg} (V) to the actual μ_a of the bottom layer was expressed by a function of the ratio of μ_a^{seg} in an earlier time segment to that in a later one. In this article we examined the relationship between the ratio of $\mu_a^{\mathrm{seg}}(\mathrm{V})$ to $\mu_{a4}[\mu_a^{\mathrm{seg}}(\mathrm{V})/\mu_{a4}]$ and the ratio of μ_a^{seg} in segment-I to that in segment-V ($\mu_a^{\mathrm{seg}}\ \mathrm{ratio}_{\mathrm{I/V}}$) obtained from Group A (Fig. 2). All data obtained from the various mediums with different sets of (d_1, d_2) were plotted together in the graph. The plot shows that the $\mu_a^{\mathrm{seg}}(\mathrm{V})/\mu_{a4}$ could be expressed as one polynomial function of the $\mu_a^{\mathrm{seg}}\ \mathrm{ratio}_{\mathrm{I/V}}$ $[\mu_a^{\mathrm{seg}}(\mathrm{V})/\mu_{a4} = -1.70(\mu_a^{\mathrm{seg}}\ \mathrm{ratio}_{\mathrm{I/V}})^2 + 4.82(\mu_a^{\mathrm{seg}}\ \mathrm{ratio}_{\mathrm{I/V}}) - 2.35]$ with an adjusted coefficient of determination $R^2 = 0.976$. The deviation of $\mu_a^{\mathrm{seg}}(\mathrm{V})/\mu_{a4}$ from the regression curve was less than 6% (mean error was 1.6%).

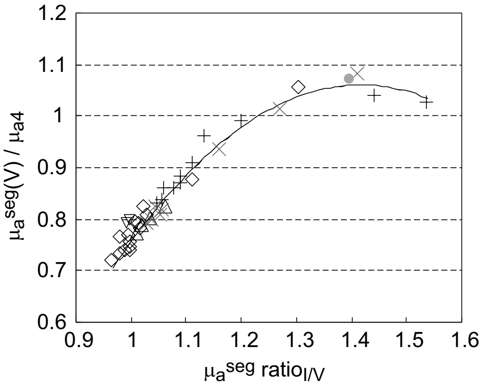

Fig. 2 The ratio of the μ_a^{seg} (V) to μ_{a4} in reference to the ratio of the μ_a^{seg} (I) to (V) ($\mu_a^{\mathrm{seg}}\ \mathrm{ratio}_{\mathrm{I/V}}$) predicted by Monte Carlo simulation in all the mediums of Group A. Different symbols represent six different sets of (d_1, d_2): (3, 5), (+); (3, 7), (∇); (4, 7), (×); (5, 7), (triangle); (5, 5), (filled circle); (5, 9), (diamond). Solid line represents the polynomial regression curve obtained from all the data.

Figure 3 is a plot of the $\mu_a^{\mathrm{seg}}(\mathrm{V})/\mu_{a4}$ versus the $\mu_a^{\mathrm{seg}}\ \mathrm{ratio}_{\mathrm{I/V}}$ for Groups B and C, where the $\mu_s{}'$ values of layers #1 and #2 are different from those in Group A. The solid line represents the regression curve of the relation between $\mu_a^{\mathrm{seg}}(\mathrm{V})/\mu_{a4}$ and $\mu_a^{\mathrm{seg}}\ \mathrm{ratio}_{\mathrm{I/V}}$ for the Group A results, as also shown in Fig. 2. The data points from Groups B and C are in good agreement with the regression curve obtained from the data sets of Group A (an adjusted $R^2 = 0.975$). The deviation of $\mu_a^{\mathrm{seg}}(\mathrm{V})/\mu_{a4}$ in Groups B and C from the regression curve was less than 8% (mean error was 2.7%). This result suggests the conclusion that the relation between $\mu_a^{\mathrm{seg}}(\mathrm{V})/\mu_{a4}$ and the $\mu_a^{\mathrm{seg}}\ \mathrm{ratio}_{\mathrm{I/V}}$ can be expressed by $[-1.70(\mu_a^{\mathrm{seg}}\ \mathrm{ratio}_{\mathrm{I/V}})^2 + 4.82(\mu_a^{\mathrm{seg}}\ \mathrm{ratio}_{\mathrm{I/V}}) - 2.35]$ irrespective of the $\mu_s{}'$ values of the upper layers.

4.3 *Temporal Variations in the s-mPPL in Each Layer*

Figures 4(a) and 4(b) show temporal variations in the s-mPPL in the four layers. In the medium where μ_{a4} was larger than μ_{a2}

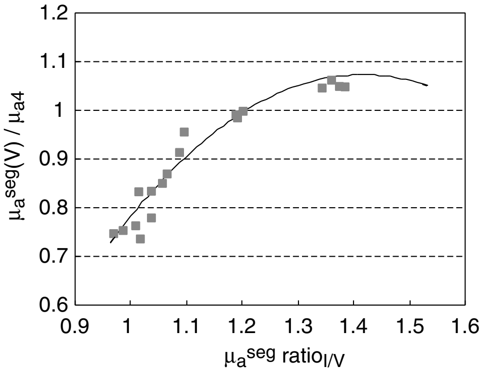

Fig. 3 The ratio of the μ_a^{seg} (V) to μ_{a4} in reference to the ratio of the μ_a^{seg} (I) to (V) ($\mu_a^{\mathrm{seg}}\ \mathrm{ratio}_{\mathrm{I/V}}$) predicted by Monte Carlo simulation in all the mediums in Groups B and C, where $\mu_s{}'$ values of layers #1 and #2 were different from those in Group A. Solid line, which is the same as that in Fig. 2, represents the regression curve obtained from the data sets of Group A.

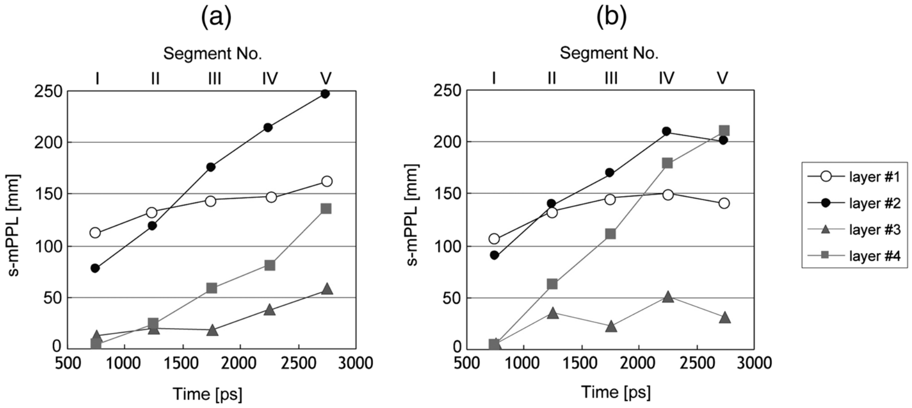

Fig. 4 Temporal variations of s-mPPL predicted by the Monte Carlo simulation at each layer of #1–#4 in two four-layered mediums in Group A. (a) $\mu_{a1} = 0.015\ \mathrm{mm}^{-1}$, $\mu_{a2} = 0.012\ \mathrm{mm}^{-1}$, $\mu_{a4} = 0.02\ \mathrm{mm}^{-1}$, $(d_1, d_2) = (5, 5)$; (b) $\mu_{a1} = 0.015\ \mathrm{mm}^{-1}$, $\mu_{a2} = 0.012\ \mathrm{mm}^{-1}$, $\mu_{a4} = 0.01\ \mathrm{mm}^{-1}$, $(d_1, d_2) = (5, 5)$The s-mPPL in each layer was calculated by (the sum of the mPPL/mTPL in each depth within the corresponding layer) × (the midpoint time in each time segment) × (light velocity in the mediums).

[Fig. 4(a)], the s-mPPLs in layers #2 and #4 markedly increased with time, and the s-mPPL in layer #2 was the longest in the latter time segments. The temporal changes in s-mPPL in layer #1, which was longer than that in layer # 4, was small compared to those in layers #2 and #4. The s-mPPL in layer #3, which was the shortest, also showed small increments with time.

In the medium where μ_{a4} was smaller than μ_{a2} [Fig. 4(b)], the s-mPPL in layer #4 markedly increased with time, with a steeper slope than that in the medium in Fig. 4(a). The s-mPPLs in layer #2 increased with time in time segments I–IV, with amplitudes very similar to those in Fig. 4(a). In time segment-V, however, the s-mPPL in layer #2 did not increase. The temporal variations in the s-mPPLs in layers #1 and #3 were relatively small, especially after time segment-III.

4.4 *Phantom Experiment*

Figures 5(a) and 5(b) show the profiles of the time-resolved reflectances of the object [I(t)] and reference [I$_R(t)$] at 760 nm, which were deconvoluted by the incident light, and the $A^{\text{diff}} - t$ curve, respectively. The profiles of $A^{\text{diff}}(t)$ were reliable in the time range of 0.5 to 3 ns (segments-I to -V). From Fig. 5(b), $\mu_a^{\text{seg}}(\text{I})$ and $\mu_a^{\text{seg}}(\text{V})$ were estimated at each measurement position. Substituting these values into the function $[\mu_a^{\text{seg}}(\text{V})/\mu_{a4} = -1.70(\mu_a^{\text{seg}}\text{ratio}_{\text{I/V}})^2 + 4.82(\mu_a^{\text{seg}}\text{ratio}_{\text{I/V}}) - 2.35]$, μ_{a4} was estimated to be $0.0156 \pm 0.002/\mathrm{mm}$ (mean ± SD). This value was very close to the actual μ_{a4} of the object $(0.015/\mathrm{mm})$.

5 Discussion

5.1 *Characterization of μ_a^{seg} in View of the Change in s-mPPL in Each Layer*

The temporal variations in μ_a^{seg} in four-layered mediums (Fig. 1) largely agreed with the previous results for a two-layered model.[26] The μ_a^{seg} changed with the time segment, reflecting the differences in μ_a in the depth direction. The main finding is that the μ_a^{seg} values in later time segments exclusively depend on the differences between μ_{a2} and μ_{a4}. That is, the $\mu_a^{\text{seg}}(\text{V})$ accurately represents the μ_{a4} in the mediums where μ_{a2} was larger than or equal to μ_{a4} [Fig. 1(a)], whereas in mediums where μ_{a2} was smaller than μ_{a4}, the $\mu_a^{\text{seg}}(\text{V})$ was smaller than μ_{a4} even in the later time segments irrespective of μ_{a1} values [Fig. 1(b)]. In addition, the dependence of μ_a^{seg} on the upper-layer thickness varied with the difference between μ_{a2} and μ_{a4} (black versus grey symbols in Fig. 1).

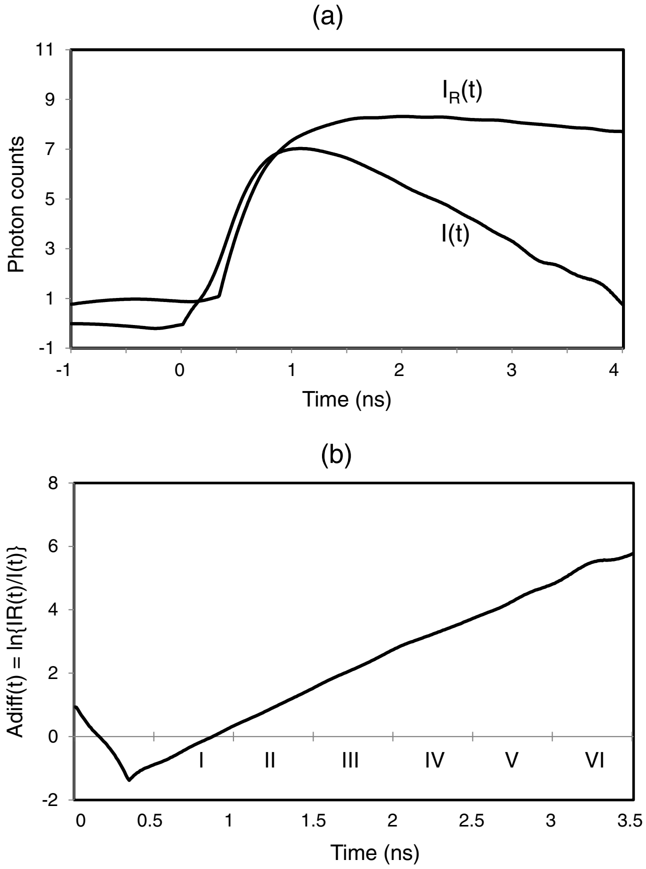

Fig. 5 Time-resolved reflectance and $A^{\text{diff}} - t$ curve obtained by phantom measurements. (a) Temporal profiles of detected light through a reference [$I_R(t)$] and an object medium [$I(t)$] on a natural logarithmic vertical scale. The time of the peak of the instrument function was taken as 0 s. The data of detected light intensity are deconvoluted by the temporal profile of the incident light. (b) A^{diff}–t curve obtained from the data in (a) in the time period of 0 to 3.5 ns. The Roman numbers show segment numbers of the curve parted every 0.5 ns to obtain the μ_a^{seg}.

As defined in Sec. 2.2, μ_a^{seg} represents the mean $\mu_a(t)$ in a segment. The μ_a^{seg} value depends on the mean temporal change in $l_i(t)$ for each time segment in the individual layers [Eq. (2)]. Therefore, a consideration of the contribution of the mean change in $l_i(t)$ to the change in $L(t)$ ($= c\Delta t$; it is constant in all the segments here) in each time segment is helpful to interpret the findings mentioned above. From Figs. 4(a) and 4(b), we can predict the mean temporal change in $l_i(t)$ and its amplitude within the segment (500 ps) by interpolation of s-mPPL between the time segments. Here, it should be noted that the temporal patterns of changes in the s-mPPLs provide more important information than the amplitude of the changes as described below.

When μ_{a2} was smaller than μ_{a4}, s-mPPL in layer #2 increased considerably in all the time ranges [Fig. 4(a)]. This implies that the contribution of the mean change in $l_2(t)$ to the change in $L(t)$ was high enough to strongly influence the μ_a^{seg} even in later time segments. This dominant change in $l_2(t)$ can explain the finding that the μ_a^{seg} at the later time represented values smaller than μ_{a4} in the mediums where μ_{a2} is smaller than μ_{a4}. The dominance of the change in $l_2(t)$ also accounts for the difference in μ_a^{seg} at later time segments between the mediums with $(d_1, d_2) = (3, 7)$ and with (5, 9). The reason why there was little effect of μ_{a1} on the temporal pattern of changes in μ_a^{seg} may be ascribed to the smaller temporal change in s-mPPL in layer #1.

When μ_{a2} was larger than μ_{a4}, μ_a^{seg} at segments-V and -VI mainly represented the μ_{a4} [Fig. 1(a)]. This is explained by the finding that there was no difference in s-mPPL in layer #2 between segment-IV and segment-V, while s-mPPL in layer #4 in segment-V was longer than that in segment-IV [Fig. 4(a)], which indicates that the contribution of the mean change in $l_2(t)$ to the change in $L(t)$ in these segments was smaller than that of $l_4(t)$. Therefore, it was concluded that the size difference between the μ_{a2} and the μ_{a4} is critical for the change in $l_i(t)$ in a later time segment, which determines μ_a^{seg} values.

5.2 *Determination of μ_a in the Bottom Layer by Correction of μ_a^{seg}*

Like in two-layered models, when the μ_a value of the bottom layer was larger than that of the upper layer, the $\mu_a^{\mathrm{seg}}(\mathrm{V})$ was smaller than the μ_{a4}. With two-layered models, the ratio of $\mu_a^{\mathrm{seg}}(\mathrm{IV})$ or (V) to the real μ_a of the lower layer is expressed by the affine function of the $\mu_a^{\mathrm{seg}}\,\mathrm{ratio}_{\mathrm{I/V}}$, which enables estimation of the μ_a of the lower layer.[26] The difference between $\mu_a^{\mathrm{seg}}(\mathrm{V})$ and μ_{a4} in the four-layered models also depends on the $\mu_a^{\mathrm{seg}}\,\mathrm{ratio}_{\mathrm{I/V}}$, though the $\mu_a^{\mathrm{seg}}(\mathrm{V})/\mu_{a4}$ was not expressed by an affine function but by a polynomial function of the $\mu_a^{\mathrm{seg}}\,\mathrm{ratio}_{\mathrm{I/V}}$ (Figs. 2 and 3). This relationship between the $\mu_a^{\mathrm{seg}}(\mathrm{V})/\mu_{a4}$ and $\mu_a^{\mathrm{seg}}\,\mathrm{ratio}_{\mathrm{I/V}}$ was independent of the $\mu_s{}'$ values and thicknesses of the layers #1 and #2. In addition to the high R^2 values, experimental measurements with the epoxy resin-based phantom support the validity of using this function, although there is no functional explanation why the relationship between $\mu_a^{\mathrm{seg}}(\mathrm{V})/\mu_{a4}$ and $\mu_a^{\mathrm{seg}}\,\mathrm{ratio}_{\mathrm{I/V}}$ in various object mediums with different conditions of the optical properties and thicknesses of the upper layers can be expressed by a single polynomial function.

5.3 *Determination of an Adequate Reference in Time Segment Analysis*

We have reported that the difference in $\mu_s{}'$ between the upper layer of the object and the reference significantly influenced the μ_a^{seg} in the time segments earlier than 2500 ps.[26] However, this difference did not influence the μ_a^{seg} after 2500 ps, and the difference in $\mu_s{}'$ between the lower layer of the object and the reference rarely affected the μ_a^{seg} values in all the time segments. The present study used a curve fitting procedure to determine the $\mu_s{}'$ value of the reference. The effect of the time range of the curve fitting on the μ_a^{seg} within the range of 250 to 3000 ps was investigated. When the $\mu_s{}'$ of the reference was determined by fitting over the wider time ranges, the plots of $\mu_a^{\mathrm{seg}}(\mathrm{V})/\mu_{a4}$ versus $\mu_a^{\mathrm{seg}}\,\mathrm{ratio}_{\mathrm{I/V}}$ did not converge on a single curve. Therefore, we used the time range of 250 to 1000 ps as the most appropriate range for fitting to determine the averaged $\mu_s{}'$ of the upper layers. However, there were no differences in $\mu_s{}'$ values of the epoxy resin-based phantom of the two fitting ranges (250 to 1000 ps and 0 to 4500 ps). In practical measurements, an inappropriate convolution process by the incident light pulse and the time lag of the pulse launching time may induce errors when deriving the $\mu_s{}'$, whereas our simulation did not include noise. This may account for the discrepancy between the simulations and the experimental results.

5.4 *Possibility of Application of the Present Method to Human Head Measurements*

As described above, practical measurements are, in general, accompanied by noises arising from various causes, such as a change in coupling between a light guide and the object's surface. In this article, we examined the applicability of the present method to practical measurements by using the four layered slab phantom. The difference between the estimated (0.0156 ± 0.002/mm) and actual μ_a values (0.015/mm) was maximally about 0.008/mm (about 5%). Considering the deviation of $\mu_a^{\mathrm{seg}}(\mathrm{V})/\mu_{a4}$ from the regression curve (Figs. 2 and 3) that was less than 8%, the estimation error is acceptable. Further, since the relationship between the $\mu_a^{\mathrm{seg}}(\mathrm{V})/\mu_{a4}$ and $\mu_a^{\mathrm{seg}}\,\mathrm{ratio}_{\mathrm{I/V}}$ was independent of the $\mu_s{}'$ values and thicknesses of the layers #1 and #2 in the range used in this study ($\mu_s{}'$ of 0.8 to 1.8/mm, thickness of less than 15 mm), it is expected that the applicability of the present approach could be extended to *in vivo* measurements.

In the adult human head, the total thickness of scalp, skull, and CSF is 11 to 15 mm in the forehead, and about 12 mm in the temporal and occipital areas.[32,33,42] Therefore, it is likely that the μ_a of the brain can be estimated by the present method on the assumption that the human head is a four-layered slab model. It is however difficult to simply apply this method to measurements in the parietal region, where the total thickness is 15 to 25 mm. Further, the four-layered slab would be too simple for a human head model. As the next step, thus, we will investigate the applicability of our "time segment analysis" to more realistic human head models with the total thickness of the extracerebral tissues in the range of 8 to 25 mm.

6 Conclusion

This study demonstrated that the "time segment analysis" of time resolved reflectance could be applied to four-layered slab models. The $\mu_a^{\mathrm{seg}}(\mathrm{V})/\mu_{a4}$ was expressed by a unique function of the μ_a^{seg} $\mathrm{ratio}_{\mathrm{I/V}}$ on the condition that the thickness of the upper layer was less than 15 mm. Since the μ_a of the bottom layer can be determined by this function, the approach reported here has the potential to selectively and quantitatively measure hemoglobin concentrations in the human brain.

Acknowledgments

The authors very much appreciate the helpful discussion with Y. Yamashita and M. Oda in Hamamatsu Photonics KK. This research was supported by Grants-in Aid for Scientific Research (C) from the Japan Society for the Promotion of Science (No. 16500468).

References

1. F. F. Jöbsis, "Noninvasive infrared monitoring of cerebral and myocardial oxygen sufficiency and circulatory parameters," *Science* **198**(4323), 1264–1267 (1977).
2. T. Takahashi et al., "Influence of skin blood flow on near-infrared spectroscopy signals measured on the forehead during a verbal fluency task," *NeuroImage* **57**(3), 991–1002 (2011).
3. E. Kirilina et al., "The physiological origin of task-evoked systemic artifacts in functional near infrared spectroscopy," *NeuroImage* **61**(1), 70–81 (2012).
4. S. Del Bianco, F. Martelli, and G. Zaccanti, "Penetration depth of light re-emitted by a diffusive medium: theoretical and experimental investigation," *Phys. Med. Biol.* **47**(23), 4131–4144 (2002).
5. J. Selb, D. K. Joseph, and D. A. Boas, "Time-gated optical system for depth-resolved functional brain imaging," *J. Biomed. Opt.* **11**(4), 044008 (2006).
6. A. Torricelli et al., "Time-resolved reflectance at null source-detector separation: improving contrast and resolution in diffuse optical imaging," *Phys. Rev. Lett.* **95**(7), 078101 (2005).
7. G. Zaccanti et al., "Optical properties of biological tissues," *Proc. SPIE* **2389**, 513–521 (1995).
8. A. Ishimaru, "Diffusion of a pulse in densely distributed scatters," *J. Opt. Soc. Am.* **68**(8), 1045–1050 (1978).
9. S. Ijichi et al., "Quantification of cerebral hemoglobin as a function of oxygenation using near-infrared time-resolved spectroscopy in a piglet model of hypoxia," *J. Biomed. Opt.* **10**(2), 024026 (2005).
10. V. Quaresima et al., "Bilateral prefrontal cortex oxygenation responses to a verbal fluency task: a multichannel time-resolved near-infrared topography study," *J. Biomed. Opt.* **10**(1), 011012 (2005).
11. Y. Hoshi et al., "Resting hypofrontality in schizophrenia: a study using near-infrared time-resolved spectroscopy," *Schizophr. Res.* **84**(2–3), 411–420 (2006).
12. A. Liebert and A. Kienle, "Light diffusion in N-layered turbid media: frequency and time domains," *J. Biomed. Opt.* **15**(2), 025002 (2010).
13. A. Kienle et al., "Investigation of two-layered turbid media with time-resolved reflectance," *Appl. Opt.* **37**(28), 6852–6862 (1998).
14. A. H. Hielscher et al., "Time-resolved photon emission from layered turbid media," *Appl. Opt.* **35**(4), 719–728 (1996).
15. A. Kienle et al., "Noninvasive determination of the optical properties of two-layered turbid media," *Appl. Opt.* **37**(5), 779–791 (1998).
16. F. Martelli et al., "Analytical approximate solutions of the time-domain diffusion equation in layered slabs," *J. Opt. Soc. Am. A* **19**(1), 71–80 (2002).
17. F. Martelli et al., "Phantom validation and in vivo application of an inversion procedure for retrieving the optical properties of diffusive layered media from time-resolved reflectance measurements," *Opt. Lett.* **29**(17), 2037–2039 (2004).
18. M. Shimada, Y. Hoshi, and Y. Yamada, "Simple algorithm for the measurement of absorption coefficients of a two-layered medium by spatially resolved and time-resolved reflectance," *Appl. Opt.* **44**(35), 7554–7563 (2005).
19. J. Steinbrink et al., "Determining changes in NIR absorption using a layered model of the human head," *Phys. Med. Biol.* **46**(3), 879–896 (2001).
20. S. R. Arridge, "Optical tomography in medical imaging," *Inverse Probl.* **15**(6), R41–R93 (1999).
21. F. Gao, P. Poulet, and Y. Yamada, "Simultaneous mapping of absorption and scattering coefficients from a three-dimensional model of time-resolved optical tomography," *Appl. Opt.* **39**(31), 5898–5910 (2000).
22. B. W. Pogue et al., "Initial assessment of a simple system for frequency domain diffuse optical tomography," *Phys. Med. Biol.* **40**(10), 1709–1729 (1995).
23. D. A. Boas et al., "The accuracy of near infrared spectroscopy and imaging during focal changes in cerebral hemodynamics," *NeuroImage* **13**(1), 76–90 (2001).
24. B. W. Zeff et al., "Retinotopic mapping of adult human visual cortex with high-density diffuse optical tomography," *Proc. Natl. Acad. Aci. U. S. A.* **104**(29), 12169–12174 (2007).
25. A. Charette, J. Boulanger, and H. K. Kim, "An overview on recent radiation transport algorithm development for optical tomography imaging," *JQSRT* **109**(17–18), 2743–2766 (2008).
26. C. Sato et al., "Extraction of depth-dependent signals from time-resolved reflectance in layered turbid media," *J. Biomed. Opt.* **10**(6), 064008 (2005).
27. Y. Nomura, O. Hazeki, and M. Tamura, "Exponential attenuation of light along nonlinear path through the biological model," *Adv. Exp. Med. Biol.* **248**, 77–80 (1989).
28. Y. Tsuchiya and T. Urakami, "Photon migration model for turbid biological medium having various shapes," *Jpn. J. Appl. Phys.* **34**, L79–L81 (1995).
29. L. Wang and S. L. Jacques, *Monte Carlo modeling of light transport in multi-layered tissues in standard C*, University of Texas/M.D. Anderson Cancer Center, Houston (1992).
30. T. J. Farrel and M. S. Patterson, "A diffusion theory model of spatially resolved, steady-state diffuse reflectance for the noninvasive determination of tissue optical properties in vivo." *Med. Phys.* **19**(4), 879–888 (1992).
31. R. C. Haskell et al., " Boundary conditions for the diffusion equation in radiative transfer," *J. Opt. Soc. Am. A Opt. Image Sci. Vis.* **11**(10), 2727–2741 (1994).
32. A. Kienle and M. S. Patterson, "Improved solutions of the steady-state and the time-resolved diffusion equations for reflectance from a semi-infinite turbid medium," *J. Opt. Soc. Am. A Opt. Image Sci. Vis.* **14**(1), 246–254 (1997).
33. K. Furutsu and Y. Yamada, "Diffusion approximation for a dissipative random medium and the applications," *Phys. Rev. E* **50**(1), 3634–3640 (1994).
34. K. Levenberg, "A method for the solution of certain problems in least squares, *Quart. Appl. Math.* **2**, 164–168 (1944).
35. D. Marquardt, "An algorithm for least-squares estimation of nonlinear parameters," *SIAM J. Appl. Math.* **11**(2), 431–441 (1963).
36. P. B. Bevington, *Data Reduction and Error Analysis for the Physical Science*, McGraw-Hill, New York (1969).
37. V. D. O Connor and D. Phillips, *Time-Correlated Single-Photon Counting*, Academic Press, London (1985).
38. F. Bevilacqua et al., "In vivo local determination of tissue optical properties: applications to human brain," *Appl. Opt.* **38**(22), 4939–4950 (1999).
39. J. H. Choi et al., "Noninvasive determination of the optical properties of adult brain: near-infrared spectroscopy approach," *J. Biomed. Opt.* **9**(1), 221–229 (2004).
40. M. Okamoto et al., "Three-dimensional probabilistic anatomical cranio-cerebral correlation via the international 10–20 system oriented for transcranial functional brain mapping," *Neuroimage* **21**(1), 99–111 (2004).
41. H. Zhao et al., "Maps of optical differential pathlength factor of human adult forehead, somatosensory motor, occipital regions at multi-wavelengths in NIR," *Phys. Med. Biol.* **47**(1), 2075–2093 (2002).
42. A. Liebert et al., "Time-resolved multidistance near-infrared spectroscopy of the adult head: intracerebral and extracerebral absorption changes from moments of distribution of times of flight of photons," *Appl. Opt.* **43**(15), 3037–3047 (2004).
43. D. A. Boas and A. M. Dale, "Simulation study of magnetic resonance imaging-guided cortically constrained diffuse optical tomography of human brain function," *Appl. Opt.* **44**(9), 1957–1968 (2005).

44. Y. Hoshi et al., "Reevaluation of near-infrared light propagation in the adult human head: implications for functional near-infrared spectroscopy," *J. Biomed. Opt.* **10**(6), 064032 (2005).
45. E. Okada and D. T. Delpy, "Near-infrared light propagation in an adult head model. I. Modeling of low-level scattering in the cerebrospinal fluid layer," *Appl. Opt.* **42**(16), 2906–2914 (2003).
46. J. Johansson et al., "Time-resolved NIR/Vis spectroscopy for analysis of solids: Pharmaceutical tablets." *Appl. Spectro.* **56**(6), 725–731 (2002).
47. T. J. Kennett, W. V. Prestwich, and A. Robertson, "Baysian deconvolution II: noise properties." *Nucl. Instr. Meth.* **151**, 293–301 (1978).